
# Concomitant Precipitation of Intermetallic β-NiAl and Carbides in a Precipitation Hardened Steel

ORIGINAL RESEARCH ARTICLE

# Concomitant Precipitation of Intermetallic $\beta$-NiAl and Carbides in a Precipitation Hardened Steel

S. JAKOB, M. HÖRNQVIST COLLIANDER, J. KAWSER, S. RASHIDI, S.W. OOI, and M. THUVANDER

The investigated steel is hardened by precipitation of both intermetallic $\beta$-NiAl particles and carbides. Around peak hardness, here reached after aging at 520 °C for 6 h, the number density of $\beta$-NiAl particles is $2.4 \times 10^{24}$ and $4.4 \times 10^{23}$ for carbides, respectively. The carbides and $\beta$-NiAl often form co-precipitates with presumably the carbides nucleating on the $\beta$-NiAl precipitates. The secondary carbides are mainly of the Cr-rich $M_{23}C_6$ type in the investigated states. The steel has a good resistance against over-aging, whereby the $\beta$-NiAl coarsen considerably slower than the carbides.

https://doi.org/10.1007/s11661-023-07291-7


## I. INTRODUCTION

THE ever-increasing demands on steel components include strength, toughness and in recent years also lightweight design. The latter can be achieved by increasing the yield strength of the material as long as the deformability can be preserved. Furthermore, the mechanical strength as well as the fatigue resistance must be maintained at operating temperatures. This requires sophisticated control of chemical composition and thermo-mechanical processing.[1] Precipitation hardening is a long-established way to improve mechanical strength. High strength in excess of 1 GPa is possible by having nano-scale clusters and precipitates in the microstructure.[2,3] Most precipitation hardening steels obtain their strength by precipitation of intermetallic particles[4–7] or nm-sized carbides.[8,9] Depending on the size and coherency of the particles, the dislocation movement is hindered either by shearing through the particle or by formation of dislocation loops around the precipitates (Orowan mechanism).[10] The investigated steel, Hybrid 55®,[11] obtains a high strength by the formation of intermetallic $\beta$-NiAl precipitates (also known as B2-NiAl for its CsCl structure) on one hand and finely dispersed carbides on the other hand. This group of steel is also called dual-hardening steels and bridges the gap between tool steels, maraging steels and lower alloyed engineering steels.[12–15] Other co-precipitation systems employ the formation of Cu precipitates alongside carbides.[16,17] A comprehensive review can be found in Reference 18. The steel in this study is fabricated using ingot casting allowing for alloying with a high content of aluminium, which in addition to formation of Al-containing intermetallic particles also provides good corrosion properties. The carbon content is elevated to facilitate the carbide formation and the microstructure consists of martensite. Hybrid 55 displays a significant increase in hardness upon aging for a few hours in the temperature range of 500 °C to 600 °C, and the resistance to over-aging is better than for typical precipitation hardening steels.[11]

Atom probe tomography (APT) is a unique technique, allowing for the investigation of nm-sized features within complex engineering alloys. It has nearly atomic spatial resolution and yields the chemical information with high sensitivity for all elements.[19]

The purpose of this study is to describe the basics of the precipitation process and to understand the reason for the good over-aging resistance. Therefore, APT was conducted on peak-hardened and over-aged specimens. Furthermore, a solution-annealed sample as well as the heat-treated materials have been investigated using synchrotron X-ray diffraction (XRD).

## II. EXPERIMENTAL

The composition of the investigated steel Hybrid 55 was measured by optical emission spectroscopy and is shown in Table I. After casting, homogenization, hot

S. JAKOB, M. HÖRNQVIST COLLIANDER, J. KAWSER, S. RASHIDI, and M. THUVANDER are with the Department of Physics, Chalmers University of Technology, 412 96 Gothenburg, Sweden. Contact e-mail: severin.jakob@chalmers.se; mattias.thuvander@chalmers.se S.W. OOI is with the Maxwell Centre, Ovako Group R&D, JJ Thompson Avenue, Cambridge, CB3 0HE, UK and also with the Ovako Corporate R&D, Building 202, 813 82 Hofors, Sweden.
Manuscript submitted June 30, 2023; accepted December 19, 2023.



Published online: 19 January 2024

rolling and soft annealing treatment, the steel was austenitized at 950 °C for 45 minutes, followed by quenching. This condition is further called solution-annealed (SA) since most of the carbides are dissolved. One aging treatment was performed at 520 °C for 6 hours to reach approximately peak hardness. Also, one over-aged sample was produced by heat treatment at 650 °C for 4 hours. The three samples are designated as SA, peak-aged and over-aged, and the hardness values were 410, 600 and 360 HV, respectively.

The APT study was carried out using a LEAP 3000X HR (Imago Scientific Instruments). The analyses were carried out in laser mode with a laser pulse energy of 0.30 nJ (frequency 200 kHz, detection rate 0.5 pct, temperature 50 K). The data were evaluated using the software IVAS 3.6 (CAMECA). Specimen preparation was made using standard electropolishing.[20] The collected datasets had mass spectra with some overlapping peaks. Especially the peak at 27 Da is of interest since it has contributions from $Fe^{2+}$, $Cr^{2+}$ and $Al^{+}$ ions. The compositions of matrix and precipitates were measured by separating the reconstruction into several POS-files. Hereby, the peak at 27 Da could be attributed to Al for intermetallic particles, Fe or Cr in case of carbides and Fe in the matrix. The composition between matrix and intermetallic particles is depicted with proximity histograms (proxigrams). There, the contribution of Fe and Cr was calculated proportionally to the peaks at 26 and 28 Da, respectively, using the natural isotope abundance. The remaining ions at 27 Da were then attributed to Al. The peak at 24 Da contains $C_2^{+}$ and $C_4^{2+}$. Since there is a peak at 24.5 Da for $C_4^{2+}$ and the peak decomposition revealed a majority of $C_4^{2+}$ for 24 Da, this peak was ranged accordingly. The peak at 29 Da was ranged as $Ni^{2+}$. Size, volume fraction and number density of the precipitates were calculated using iso-concentration surfaces as well as the parameter-free method presented by Zhao *et al.*[21] This method uses the radial distribution function (RDF) of the atomic species. The size of the precipitates was then calculated from the number of atoms, hence, avoiding local magnification effects.[22,23] In this study, only the RDF of Ni was used for $\beta$-NiAl precipitates to avoid the overlap of Al at 27 Da.

To obtain crystallographic information, XRD measurements were made at the Swedish Material Science beamline P21 at the PETRA III synchrotron (DESY, Germany). The energy was 60 keV, corresponding to a wavelength $\lambda = 0.2066$ Å. Two VAREX XRD4343CT area detectors were placed downstream at a sample-to-detector distance of around 2.8 m (the exact distance was calibrated using a LaB6 standard) to allow collection of diffraction patterns in transmission. The investigated samples had a thickness of 1.0 mm, and the beam size was $0.5 \times 0.5$ mm$^2$. Data reduction was performed using PyFAI 0.20.0.[24,25]

**Table I. The Measured Chemical Composition of the Investigated Steel (in Wt. Pct), Balance Fe.[11]**

| C | Si | Mn | Cr | Ni | Mo | V | Al | Cu |
|---|---|---|---|---|---|---|---|---|
| 0.18 | 0.10 | 0.31 | 5.05 | 6.09 | 0.69 | 0.49 | 2.36 | 0.17 |

## III. RESULTS

Figure 1 shows electron micrographs of Hybrid 55. It has a martensitic microstructure with several undissolved carbides visible. The carbides are Cr-rich in case of $M_{23}C_6$ and V-rich in case of MC. The intermetallic particles as well as strength-enhancing smaller carbides are not visible at this length scale. Thus, advanced investigation methods like synchrotron XRD and APT are employed.

Figure 2 shows diffractograms obtained before and after aging. The SA condition shows clear peaks from retained austenite, weight fraction of around 2.6 pct from Rietveld refinement, which is reduced to 0.8 pct after 6 hours at 520 °C and almost zero (too low for

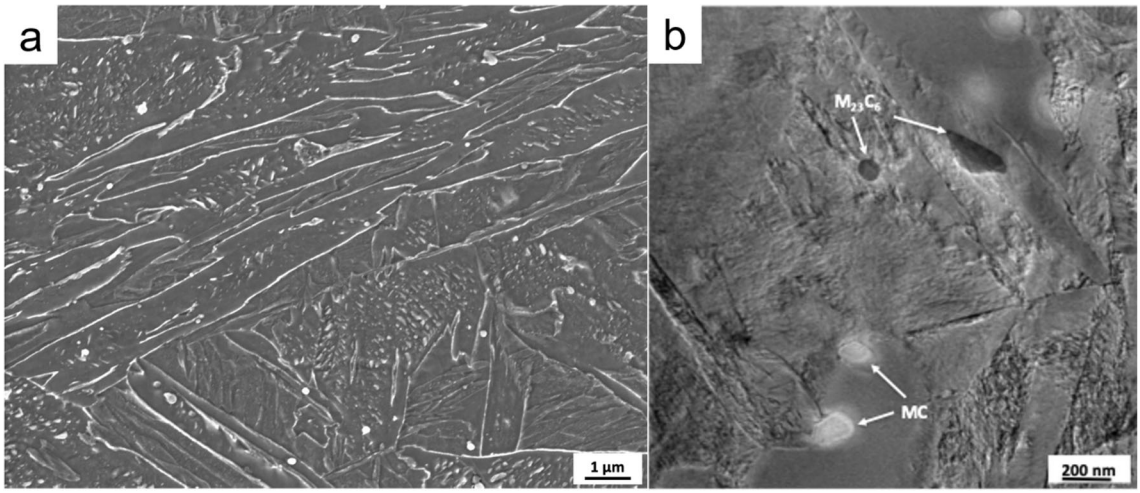


Fig. 1—Electron micrographs ((*a*) SEM and (*b*) TEM) of the Hybrid 55 microstructure. Only undissolved carbides are visible at the magnifications used here.

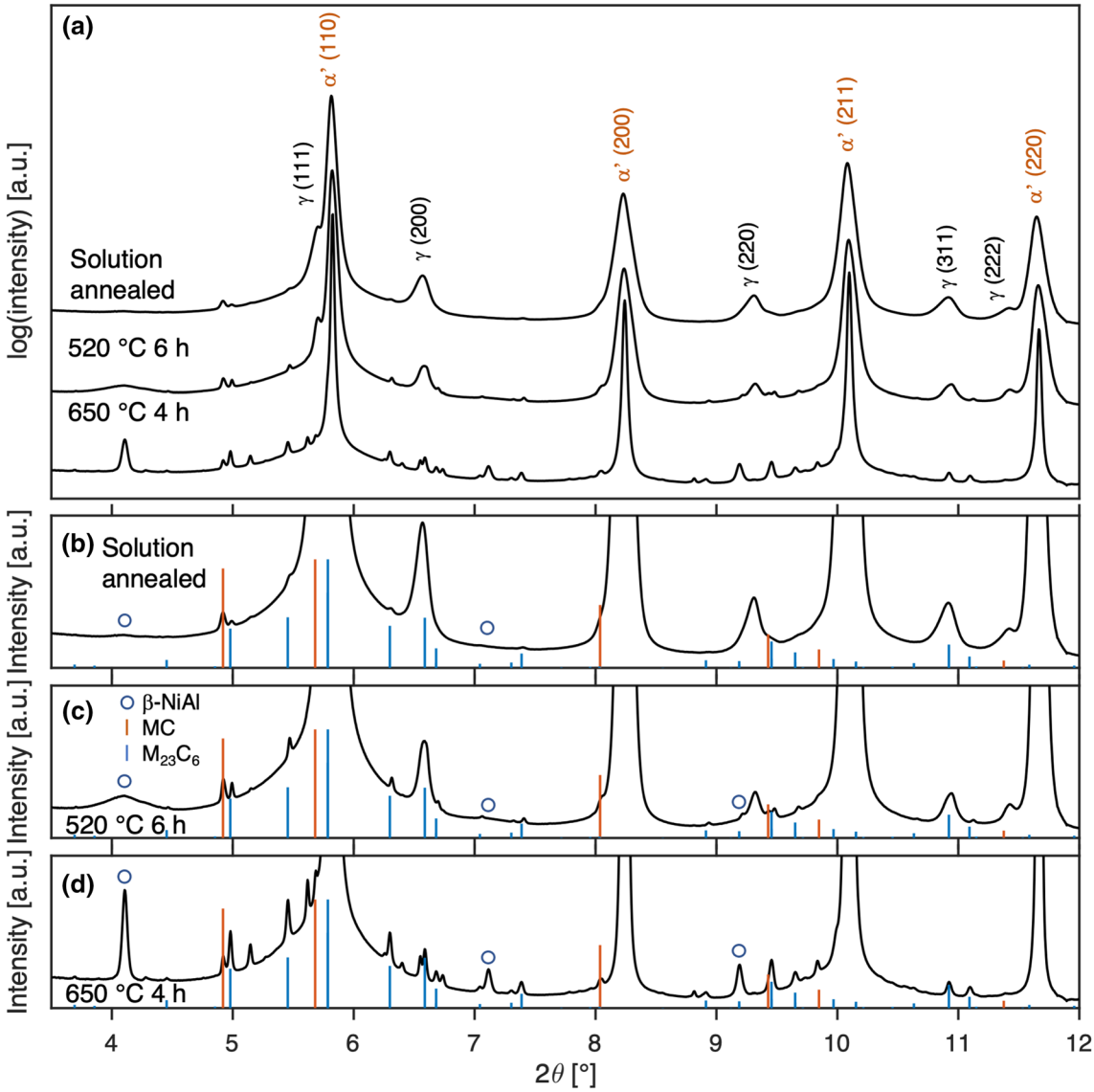


Fig. 2—(*a*) XRD diffractogram of material in the solution-annealed state, and after aging at 520 °C for 6 h and 650 °C for 4 h (logarithmic intensity scale and vertical offsets). (*b*) through (*d*) Magnified views with linear intensity scales to highlight carbides and NiAl (Color figure online).

reliable quantification) after 4 hours at 650 °C (Figure 2(a)). A closer examination of the SA condition (Figure 2(b)) shows the presence of both MC and $M_{23}C_6$. The carbide peaks are relatively sharp, indicating particle sizes above where size-related broadening occurs. This is confirmed by TEM, as seen in Figure 1, where scarce MC and $M_{23}C_6$ carbides larger than 100 nm are observed.

The $\beta$-NiAl particles are clearly visible after 6 hours at 520 °C (Figure 2(c)), although the peaks remain broad, which indicates a small particle size. An approximate size, $D$, of the coherently diffracting domains can be obtained from the Scherrer equation

$$D = \frac{0.9\lambda}{W\cos\theta}, \qquad [1]$$

where $W$ is the full width at half maximum (after subtraction of the instrumental peak width) and $\theta$ is the Bragg angle. For the peak-aged condition, Eq. [1] suggests an approximate diameter of around 3 nm. No significant change of the MC peaks could be observed, whereas the $M_{23}C_6$ peaks increased significantly in intensity (see Figure 3), indicating an increased volume fraction.

In the over-aged condition there is a significant increase in the $M_{23}C_6$ fraction, as suggested by the integrated peak area (Figure 3), and a clear narrowing of the $\beta$-NiAl peak (Figures 2(a) and (c)). The integrated intensity of the $\beta$-NiAl peak is not significantly higher compared to the peak-aged condition, only around 5 pct, but the peak width is distinctly smaller, and Eq. [1] results in an approximate diameter of 25 nm for the over-aged condition. There are also several additional

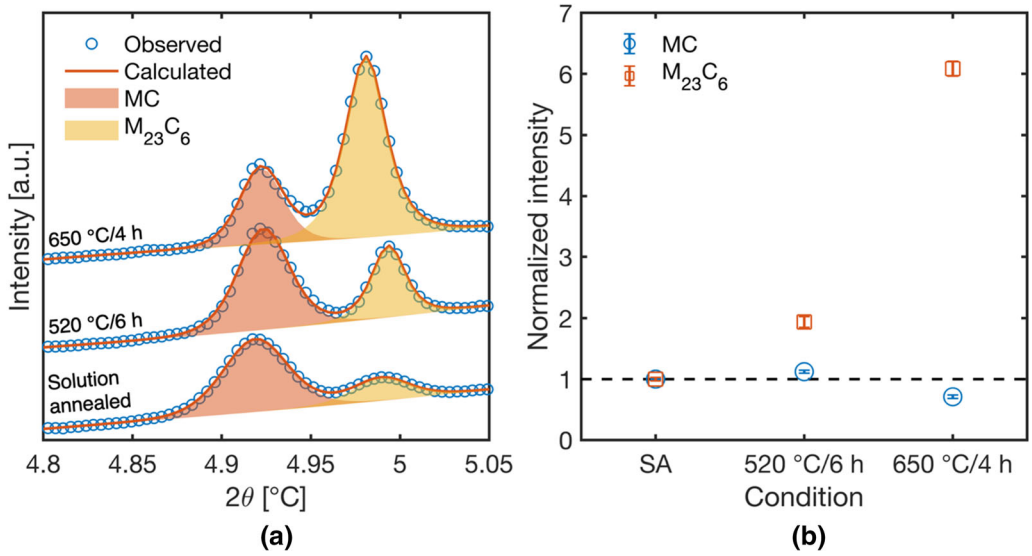


Fig. 3—(*a*) Single peak fits of MC and $M_{23}C_6$ peaks for the different conditions. (*b*) Integrated intensities of the fitted peaks, normalized by the value for the SA condition (Color figure online).

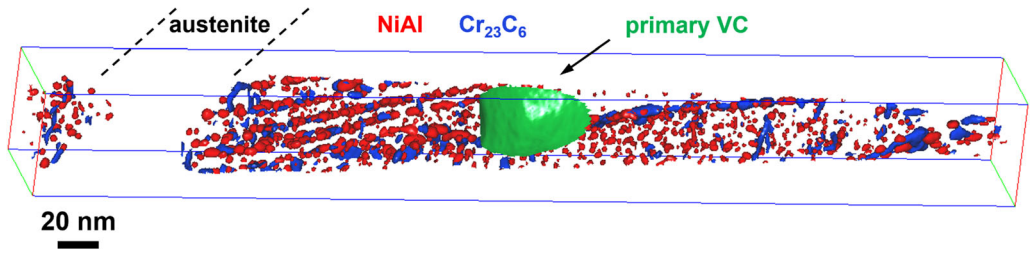


Fig. 4—APT reconstruction of the peak-aged material (520 °C/6 h) showing co-precipitation of *β*-NiAl (red iso-surfaces) and $Cr_{23}C_6$ (blue iso-surfaces). A large primary VC is shown in green (Color figure online).

diffraction peaks, likely a result of the precipitation of other carbide species. As the over-aged condition is mainly included for comparison in the present case, no further attempts were made to identify the additional carbides.

The APT investigation of the peak-aged (520 °C/6 hours) sample reveals a very large number density of small precipitates, see Figure 4. The precipitates are of two types; *β*-NiAl and $Cr_{23}C_6$. The particles are displayed as iso-concentration surfaces. The thresholds are 25 at. pct Ni and Al for the intermetallic particles, 12 at. pct Cr for $Cr_{23}C_6$ and 30 at. pct V for a primary VC, respectively. Most of the carbides are in contact with a *β*-NiAl particle. The precipitates were partly aligned on parallel planes, presumably consisting of arrays of dislocations. Furthermore, a 50 nm wide section without any precipitates can be seen in Figure 4. This volume is most probably retained austenite. The interface is enriched in carbide forming metals as well as P, suggesting a former grain boundary. Throughout the precipitation-free region, alloying elements, such as Al, Cr, Ni and C are enriched. From the APT analysis, it cannot be confirmed whether this volume transformed to martensite upon final cooling (after the aging). See the supplementary file for atom distribution maps.

In the over-aged sample (650 °C/4 hours), coarsening of the precipitates has occurred, see the APT reconstructions in Figure 5. The carbides were of two distinct types; $Cr_{23}C_6$ and VC. The iso-concentration surface thresholds for the depicted particles are 25 at. pct Ni and Al for the intermetallic particles, 12 at. pct Cr for $Cr_{23}C_6$ and 6 at. pct V for VC, respectively. The carbides always have at least one *β*-NiAl particle in direct contact with them, but many *β*-NiAl particles are isolated. Elemental distributions can be found in the Supplementary File.

The composition of matrix and precipitates was deduced from separated POS-files and can be seen in Table II. The *β*-NiAl precipitates still contain significant amounts of Fe and almost equal amounts of Ni and Al. The nm-sized $Cr_{23}C_6$ still incorporate large amounts of Fe, and are enriched in V and Mo. The primary VC contains small amounts of Cr and Mo. In the over-aged material, the intermetallic particles contain about 8 at. pct Fe, as well as slightly more than 2 at. pct of Cu and Mn combined. The $Cr_{23}C_6$ have higher concentration of Cr and V compared to the peak-aged condition. Also, the measured C content is higher. The VC particles have

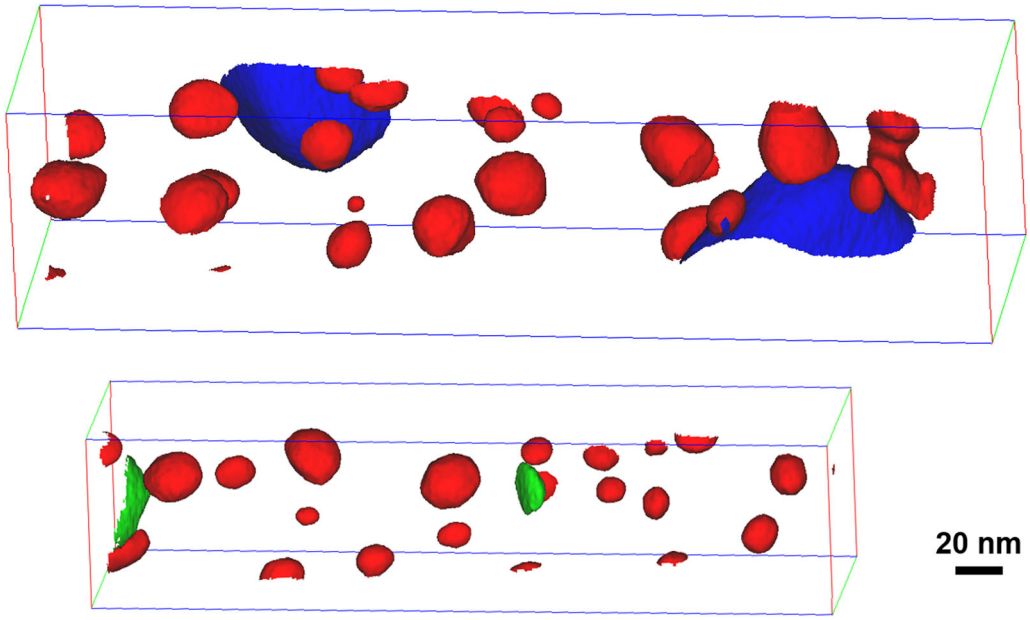


Fig. 5—APT reconstructions of two specimens from over-aged material (650 °C/4 h). The red iso-surfaces depict $\beta$-NiAl particles, the blue iso-surfaces are $Cr_{23}C_6$ and VC are depicted in green (Color figure online).

about the same amount of V and C with significantly more Cr, Mo and Fe concentration than the primary VC.

Figure 6(a) depicts the size distribution of particles derived from iso-surfaces for both peak-aged and over-aged samples. Herein, 25 at. pct of Ni and Al, and 12 at. pct of Cr were used for iso-surface calculations in IVAS, for $\beta$-NiAl and carbides, respectively. A mean equivalent radius of spherical particles was calculated and the results are listed in Table III. The error margins for these radii are calculated from variation of the threshold value by 2 at. pct Ni and Al and 1 at. pct Cr in either direction. Figure 6(b) shows the normalised RDF for Ni–Ni and Cr–Cr pairs. From this data, particle sizes can be calculated and are presented in Table III. The errors represent the 95 pct confidence interval of the fitted radius to the measured RDF.

The equivalent radii of $\beta$-NiAl precipitates derived from iso-surface volumes are in reasonable agreement with the RDF method. The size increases by more than a factor of 5 in both cases between peak-aged and over-aged condition. The numbers are also in very good agreement with those obtained from XRD. Within the analysed volume of over-aged material, $Cr_{23}C_6$ sizes (diameters) are larger than 20 nm, which is an increase by more than one order of magnitude. Volume fractions and number densities were determined from the iso-surface volumes (including edge precipitates). The volume fraction of intermetallic $\beta$-NiAl was slightly higher (6.9 pct) in peak-aged than in the over-aged condition (6.6 pct). This can be understood from higher solubility at the higher aging temperature. The threshold variation shows a broad range for peak-aged volume fraction due to the diffuse interface between matrix and precipitate. The number density of $\beta$-NiAl precipitates was about 200 times higher in the peak-aged condition. Even more so, the number density of carbides is much higher in the peak-aged condition. In the specimen of over-aged material, the carbides were measured only in part due to the limited field of view and the small analysis volume. It is not reasonable to calculate number densities from this limited sample volume, but it seems to be in the order of $10^{20}$ $m^{-3}$.

The chemical composition of $\beta$-NiAl precipitates was further investigated with proxigrams. Figure 7 depicts the chemical concentration of important elements as a function of distance to the 25 at. pct Ni + Al iso-surface. The $\beta$-NiAl particles have a gradual change in composition from the matrix. Beside the main constituents, Mn and Cu are incorporated within the precipitates. Fe and Cr are decreasing the further the distance inwards. The chemical composition of $\beta$-NiAl in the over-aged condition (Figure 7(b)) has a higher amount of Ni and Fe, whereas Al is reduced. Mn and Cu are enriched at 1.5 and 1.0 at. pct, respectively, whereas Cr is almost zero at the plateau value.

## IV. DISCUSSION

APT is a powerful technique for the detection of clusters and small precipitates. The chemical information is recorded, and size and number densities of particles can be extracted. However, the analysis is complex and different challenges must be addressed. In the case of dual-hardening steels, like Hybrid 55 in this study, Fe, Cr and Al are integral parts of the alloy and have isotopes that share the same mass-to-charge ratio. Hence, the peak in the mass spectrum at 27 Da has to be treated carefully. Since the reconstruction can be separated into different POS-files, the different regions of interest can be individually analysed, which was done in

**Table II. Average Composition of Matrix and Precipitates as Calculated from Separated POS-Files.**

| | C | Al | Si | V | Cr | Mn | Fe | Ni | Cu | Mo | M/C |
|---|---|---|---|---|---|---|---|---|---|---|---|
| | At. Pct | | | | | | | | | | (V + Cr + Fe + Mo) |
| Peak-Aged | | | | | | | | | | | |
| Matrix | 0.18 | 0.72 | 0.08 | 0.14 | 3.59 | 0.10 | 93.5 | 1.48 | 0.01 | 0.12 | |
| NiAl | 1.00 | 30.3 | 0.12 | 0.26 | 2.46 | 1.07 | 36.2 | 27.7 | 0.73 | 0.16 | |
| $Cr_{23}C_6$ | 13.8 | 0.60 | 0.22 | 2.43 | 29.3 | 0.34 | 49.0 | 1.89 | 0.03 | 2.22 | 6.01 |
| Primary VC | 47.7 | 0.03 | 0.03 | 44.5 | 3.71 | 0.02 | 0.11 | 0.48 | 0.00 | 3.30 | 1.08 |
| Austenite | 0.64 | 4.02 | 0.13 | 0.32 | 5.06 | 0.23 | 84.2 | 4.94 | 0.10 | 0.33 | |
| Over-Aged | | | | | | | | | | | |
| Matrix | 0.04 | 0.09 | 0.20 | 0.39 | 3.91 | 0.20 | 92.1 | 2.50 | 0.06 | 0.43 | |
| NiAl | 0.20 | 42.2 | 0.09 | 0.05 | 0.23 | 1.25 | 9.26 | 45.4 | 1.00 | 0.02 | |
| $Cr_{23}C_6$ | 16.9 | 0.01 | 0.01 | 5.34 | 56.5 | 0.54 | 17.5 | 0.69 | 0.00 | 2.42 | 4.84 |
| VC | 35.9 | 0.36 | 0.04 | 33.1 | 15.0 | 0.42 | 4.42 | 1.05 | 0.00 | 9.05 | 1.72 |

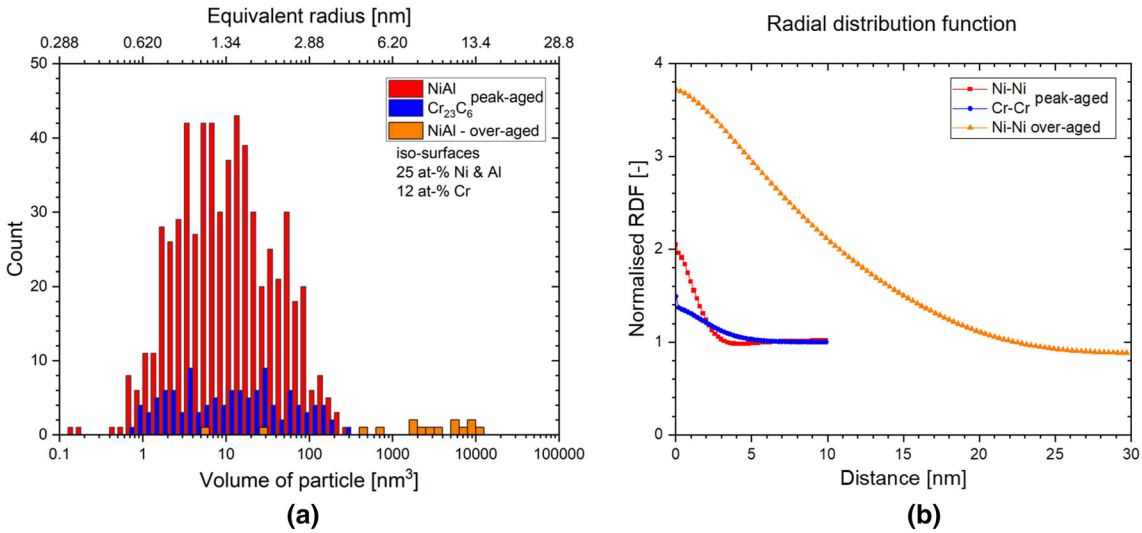


Fig. 6—(*a*) Size distribution of particles obtained using iso-surfaces; (*b*) normalised RDF of Ni–Ni and Cr–Cr pairs, respectively. Mean precipitate sizes can be deduced, see text (Color figure online).

**Table III. Mean Radii, Volume Fractions and Number Densities of the Different Precipitates in the Investigated Samples; Iso-Surface Threshold Values were 25 ± 2 at. pct Ni & Al and 12 ± 1 at. pct Cr, respectively.**

| | $R_{RDF}$ [nm] | $R_{Iso\text{-}surface}$ [nm] | Volume Fraction [Pct] | Number Density [$10^{21}$ $m^{-3}$] |
|---|---|---|---|---|
| Peak-Aged | | | | |
| NiAl | 1.41 ± 0.03 | (1.94) 1.84 (1.76) | (9.6) 6.9 (5.0) | (2700) 2400 (2100) |
| $Cr_{23}C_6$ | 1.82 ± 0.09 | (1.99) 1.99 (2.06) | (2.4) 1.8 (1.4) | (500) 440 (350) |
| Over-Aged | | | | |
| NiAl | 10.74 ± 0.08 | (9.82) 9.58 (9.25) | (6.8) 6.6 (6.3) | (14) 13 (12) |

this study. A common method to visualise composition at interfaces or iso-concentration surfaces from particles are proxigrams. In this case, the reconstruction can not be separated and the peak at 27 Da was decomposed in proportion to the main isotopes of $Fe^{2+}$ at 28 Da and $Cr^{2+}$ at 26 Da, for each point of the proxigrams. Another challenge is the measurement of phases with high evaporation fields, notably carbides. Carbon tends to diffuse on the surface of the tip. Evaporation happens often of several ions or molecules, resulting in a higher ratio of multiple hits at the detector as well as detection of $C_2$, $C_3$ and $C_4$ ions. Multiple hits in close proximity in time and space at the detector cannot be resolved and therefore the atom species is underestimated in the

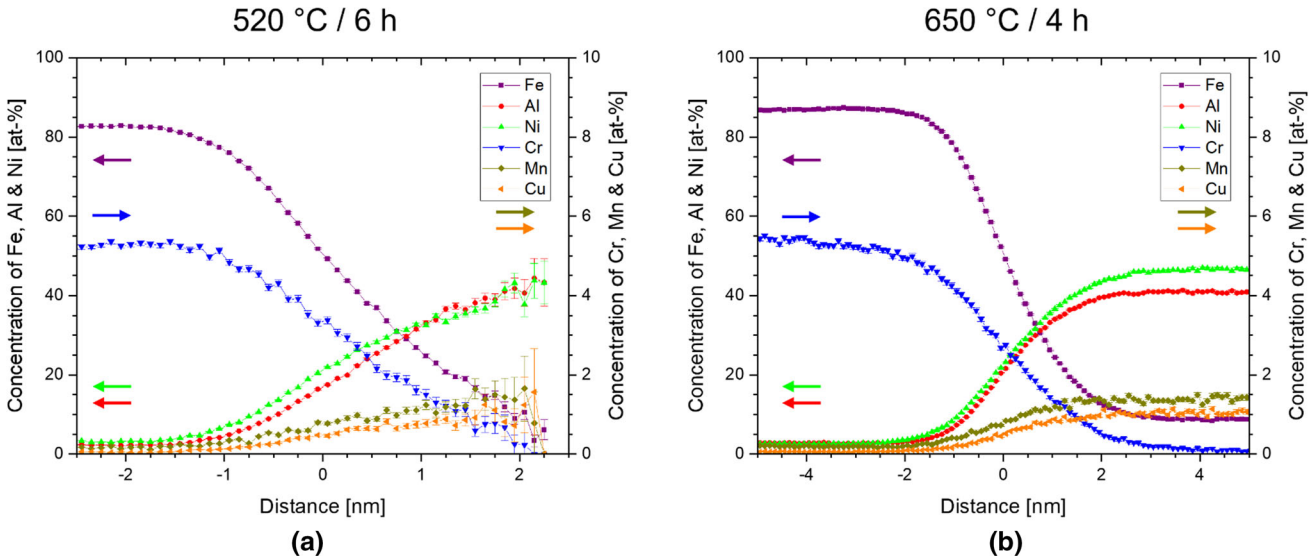


Fig. 7—Proxigrams of $\beta$-NiAl precipitates in (*a*) peak-aged and (*b*) over-aged material. Iso-surface values are 25 at. pct Ni and Al. Note the different scales on the abscissas (Color figure online).

chemical composition.[26,27] Local magnification, *i.e.,* the distortion of the reconstruction due to different evaporation fields of different phases in the material, as well as lateral resolution, limits the depiction of a sharp interface of $\beta$-NiAl particles. Additionally, Fe atoms are measured within the precipitate from the surrounding matrix. Lattice parameter estimation from the $\beta$-NiAl (100) peak in the diffractograms in Figure 2 yields 2.89(9) Å for the peak-aged condition. This is slightly larger than the nominal value of 2.881 Å (Crystallography Open Database COD ID 9008802), indicating a composition close to pure NiAl, but may indeed suggest a larger presence of Fe as the lattice parameter will increase with Fe content. Pike *et al.*[28] investigated a wide range of compositions of (Ni,Fe)Al alloys and typically found lattice parameters ranging from 2.886 to 2.889 Å for Fe concentrations in the range 15 to 40 at. pct, increasing with increasing Fe content.

In the over-aged condition, the composition in the proxigram reaches plateau values. Therefore, it is reasonable to assume a real Fe content of about 8 at. pct in the intermetallic precipitate. This is consistent with the measured lattice parameter, 2.88(3) Å, which is rather close to the nominal, indicating a lower Fe content. The size evaluation of particles was done as well by the parameter-free method of Zhao *et al.*,[21] where subjective influence of the examiner is avoided. Only the Ni–Ni RDFs (and Cr–Cr RDF for carbides) were used since Al has an overlap at one of its main peaks (27 Da). The RDF method provides similar particle sizes as when using iso-concentration surfaces. In the latter case, the iso-value is chosen by the examiner and influences the determined size. Also, since edge particles are excluded in the size distribution, a higher proportion of larger carbides is omitted. This is not the case for the more isolated $\beta$-NiAl particles.

In the peak-aged condition, the primary VC has nearly stochiometric composition with little Cr and Mo content. The Cr-carbide particles have almost 50 at. pct Fe in them. However, since they are nm-sized, a significant matrix contribution due to lateral resolution and local magnification is expected. Since C is often underestimated in APT experiments, a physical composition matching the $M_{23}C_6$ type is reasonable. This type of carbide is also found in cold-work tool steel after tempering.[29] The measured composition of $Cr_{23}C_6$ in the over-aged condition displayed a higher C content, which might result from a smaller amount of Fe from matrix contribution, since the size of the carbides are significantly larger. The V-carbide in this material has about the same amounts of V and C. However, there is also about 15 at. pct Cr and 9 at. pct Mo within the carbides. In literature, it has been shown that $M_2C$ can be reached after long aging times, however, with M = Cr or Mo.[30,31] The phase diagram of Fe–Cr–V–C suggests the existence of $M_3C$ and $M_7C_3$ beside MC and $M_{23}C_6$ at 700 °C.[32,33] Though, the carbide in this study has about 33 at. pct V, which is more than suggested to substitute Fe and Cr in $M_7C_3$.[34] The metal to carbon ratio is already below 2 (see Table II) without taking the underestimation of C in APT into account. Transition metal carbides are reported to have a wide range of carbon deficiency without a change in crystal structure.[35,36] Hence, it is reasonable to assume an under-stochiometric $MC_x$ ($x < 1$) type for this carbide. No other carbides are seen in APT, which, in combination with the narrow peak width in the diffractograms, indicates that they are larger and more scarcely distributed than the $M_{23}C_6$. Hence, no significant contribution to strengthening is expected.

The high strength of this material is based on the high number of nm-sized particles. On one hand, the intermetallic $\beta$-NiAl have coherent interfaces and dislocations should be able to move through the particles. The strength contribution can therefore be described in the simple model from Gerold and Haberkorn[37] as

$$\Delta\tau \propto f^{1/2} \cdot r^{1/2}, \quad [2]$$

where $\Delta\tau$ is the strength increase, $f$ the volume fraction and $r$ the particle radius. From Eq. [2] it can be seen that the $\beta$-NiAl precipitates contribute about the same increase in strength between the investigated conditions or even more to the overall strength in the over-aged condition. On the other hand, $Cr_{23}C_6$ is assumed to contribute by the Orowan mechanism, causing dislocation loops. The strength increase can be described by Eq. [3].[38]

$$\Delta\tau \propto \frac{G \cdot b}{\lambda} \cdot \ln\left(\frac{\lambda}{b}\right) \quad [3]$$

with $G$ the shear modulus, $b$ the Burgers vector and the interparticle spacing $\lambda$ defined as follows:

$$\lambda = N^{-1/3} - 2 \cdot r, \quad [4]$$

where $N$ is the number density of the particles. Using these equations for the $Cr_{23}C_6$ precipitates one can see that the strength contribution drops by one order of magnitude from peak-aged to over-aged condition. Since the particles are not isolated but co-precipitates in a martensitic microstructure with lath and grain boundaries, the real deformation mechanism is rather complex.

The sequence in which precipitates form is of special interest in the case of dual-hardening steels. In this study, the precipitation of intermetallic particles and carbides in Hybrid 55 was investigated in peak-aged and over-aged condition. After quenching, the alloying elements are in supersaturation. During the aging treatment, Ni and Al form clusters, which become $\beta$-NiAl intermetallic particles with Fe still incorporated.[17,30] $\beta$-NiAl exhibits coherent interfaces with the martensitic/ferritic matrix and therefore readily precipitates in a homogenous distribution of fine particles.[6,13,39,40] Carbides have an incoherent interface with the matrix. Possible nucleation sites include dislocations, lath and grain boundaries,[41] where C can agglomerate and eventually form carbides. In this dual-hardening steel the intermetallic $\beta$-NiAl precipitates are also nucleation sites for the carbides.[13,30] During formation of the intermetallic compounds other elements, such as Cr, are displaced and therefore in excess next to the $\beta$-NiAl precipitates.[6] This partition of Cr might enhance the formation of carbides as similarly observed for C next to Cu precipitates.[42] Hence, "assisted precipitation" of the secondary carbides connected to the $\beta$-NiAl particles is expected. This is visible by the fact that every carbide precipitate in the peak-aged condition is in contact with a $\beta$-NiAl particle, as can be seen in Figure 8. The small content of Cu in Hybrid 55 is found within the $\beta$-NiAl particles without clustering. It is reported that Cu prefers the Al sublattice in the B2 ordered structure, since in this way the lattice misfit to the ferritic matrix can be minimized.[43] Similarly, Mn is found within the Al sublattice.[44] This can explain the reduced Al to Ni content in over-aged precipitates. The coarsening rate of particles depend on the diffusion rate and the matrix solubility. Both factors

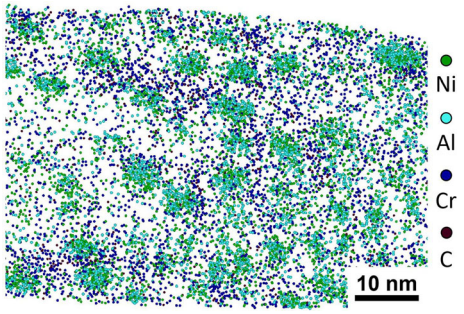


Fig. 8—Elemental distribution in a precipitation-rich plane of peak-aged material. Every $Cr_{23}C_6$ precipitate is connected to at least one $\beta$-NiAl particle.

are enhanced at higher temperatures. The possible exchange of atoms from one precipitate to the other facilitates coarsening of the particles within a short time.[43] In contrast to steels with higher alloying content of Cu, where Cu precipitates readily exchange solute atoms with $\beta$-NiAl particles, the co-precipitates in Hybrid 55 are $\beta$-NiAl and carbides. Therefore, no immediate exchange of solute elements is expected. In the over-aged state, primarily the carbides coarsen, while $\beta$-NiAl particles exhibit only a limited size increase, as was also observed in literature.[40] This is due to the quality of the interface as well as the solubility of the constituent elements. The carbides form an incoherent boundary with the matrix, whereas $\beta$-NiAl precipitates have coherent interfaces with the matrix and a misfit depending on the alloying content. Hence, more diffusion and greater driving force for coarsening is expected for the incoherent carbides. The same phenomenon was observed for Cu precipitates and carbides by Mulholland and Seidman.[31] The limited growth of the coherent intermetallic particles seems to be the reason for the improved resistance to over-aging compared to other steels for similar applications.

## V. CONCLUSIONS

The dual-hardening steel Hybrid 55 has been investigated by APT and XRD in peak-aged and over-aged condition. Peak-aging heat treatment at 520 °C for 6 hours results in high number densities of nm-sized particles of two types: intermetallic $\beta$-NiAl particles, having a mean radius of 1.4 nm and a number density of $2.4 \times 10^{24}$ m$^{-3}$ as well as $Cr_{23}C_6$ with a mean radius of 1.8 nm and number density of $4.4 \times 10^{23}$ m$^{-3}$. A precipitation-free zone corresponding to a residual austenite lath had higher alloying contents within its volume and segregation of carbide forming elements as well as traces of P at the interface.

Over-aging at 650 °C for 4 hours results in coarsening of the precipitates. However, carbides coarsen at a faster rate than the intermetallic particles. $\beta$-NiAl precipitates have a mean radius of 11 nm after this over-aging whereas carbides are measured only in part due to the limited field of view in APT. Furthermore, under-stochiometric $VC_x$ ($x < 1$) secondary carbides with

significant amounts of Mo and Cr were found in the over-aged sample material.

Every carbide is in contact with at least one intermetallic particle, indicating the heterogenous nucleation of carbides and co-precipitation of the two types of precipitates. The different character of the interfaces seems to be the reason for the divergent coarsening rates.

## ACKNOWLEDGMENTS

The Swedish Innovation Agency VINNOVA is kindy acknowledge for funding through the Grant 2018-04433. This research was performed in part at the Chalmers Materials Analysis Laboratory, CMAL. We acknowledge DESY (Hamburg, Germany), a member of the Helmholtz Association HGF, for the provision of experimental facilities. Parts of this research were carried out at beamline P21.2 at PETRA III and we would like to thank Ulrich Lienert and Sylvio Haas for assistance. Beamtime was allocated for proposal I-20190135 EC. SJ gratefully acknowledges Dr. Kristina Lindgren, now at RISE Research Institutes of Sweden, for discussions regarding the calculation of particle size and the RDF method.

## FUNDING

Open access funding provided by Chalmers University of Technology.

## CONFLICT OF INTEREST

The authors declare that they have no conflict of interest.

## OPEN ACCESS



## SUPPLEMENTARY INFORMATION

The online version contains supplementary material available at https://doi.org/10.1007/s11661-023-07291-7.

## REFERENCES

1. J. Zhao and Z. Jiang: *Prog. Mater. Sci.*, 2018, vol. 94, pp. 174–242. https://doi.org/10.1016/J.PMATSCI.2018.01.006.
2. H.J. Kong and C.T. Liu: *Technologies.*, 2018, vol. 6, p. 36. https://doi.org/10.3390/TECHNOLOGIES6010036.
3. Z. Xiong, I. Timokhina, and E. Pereloma: *Prog. Mater. Sci.*, 2021, vol. 118, 100764https://doi.org/10.1016/J.PMATSCI.2020.100764.
4. M. Hättestrand, J.-O. Nilsson, K. Stiller, P. Liu, and M. Andersson: *Acta Mater.*, 2004, vol. 52, pp. 1023–037. https://doi.org/10.1016/j.actamat.2003.10.048.
5. R.F. Decker, S. Floreen, R.K. Wilson, Maraging steels: recent developments and applications, in *Proceedings of Symposium on TMS Annual Meeting*, 1988, pp. 1–38.
6. D.H. Ping, M. Ohnuma, Y. Hirakawa, Y. Kadoya, and K. Hono: *Mater. Sci. Eng. A*, 2005, vol. 394, pp. 285–95. https://doi.org/10.1016/J.MSEA.2004.12.002.
7. Z. Guo, W. Sha, and D. Vaumousse: *Acta Mater.*, 2003, vol. 51, pp. 101–16. https://doi.org/10.1016/S1359-6454(02)00353-1.
8. C.Y. Chen, H.W. Yen, F.H. Kao, W.C. Li, C.Y. Huang, J.R. Yang, and S.H. Wang: *Mater. Sci. Eng. A*, 2009, vol. 499, pp. 162–66. https://doi.org/10.1016/J.MSEA.2007.11.110.
9. W.B. Lee, S.G. Hong, C.G. Park, K.H. Kim, and S.H. Park: *Scr. Mater.*, 2000, vol. 43, pp. 319–24. https://doi.org/10.1016/S1359-6462(00)00411-5.
10. P.M. Kelly: *Int. Metall. Rev.*, 1973, vol. 18, pp. 31–37. https://doi.org/10.1179/IMTLR.1973.18.1.31.
11. J.-E. Andersson, F. Lindberg, and P. Ölund: *Light. Des. Worldw.*, 2019, vol. 12, pp. 34–39. https://doi.org/10.1007/s41777-018-0063-3.
12. W.M. Garrison and M.S. Bhat: *Metall. Trans. A*, 1988, vol. 19A, pp. 1751–60. https://doi.org/10.1007/BF02645143.
13. F. Danoix, R. Danoix, J. Akre, A. Grellier, and D. Delagnes: *J. Microsc.*, 2011, vol. 244, pp. 305–310. https://doi.org/10.1111/J.1365-2818.2011.03537.X.
14. C.Y. Huang and H.W. Yen: *Mater. Charact.*, 2021, vol. 178, 11-1216https://doi.org/10.1016/j.matchar.2021.111216.
15. M. Hofinger, M. Staudacher, M. Ognianov, C. Turk, H. Leitner, and R. Schnitzer: *Micron*, 2019, vol. 120, pp. 48–56. https://doi.org/10.1016/j.micron.2019.02.004.
16. Y.C. Lin, I.E. McCarroll, Y.T. Lin, W.C. Chung, J.M. Cairney, and H.W. Yen: *Acta Mater.*, 2020, vol. 196, pp. 516–27. https://doi.org/10.1016/j.actamat.2020.06.046.
17. M. Hofinger, C. Turk, M. Ognianov, H. Leitner, and R. Schnitzer: *Mater. Charact.*, 2020, vol. 160, 110126https://doi.org/10.1016/j.matchar.2020.110126.
18. Z.B. Jiao, J.H. Luan, M.K. Miller, Y.W. Chung, and C.T. Liu: *Mater. Today*, 2017, vol. 20, pp. 142–54. https://doi.org/10.1016/J.MATTOD.2016.07.002.
19. W. Lefebvre-Ulrikson, F. Vurpillot, and X. Sauvage, eds.: *Atom Probe Tomography: Put Theory Into Practice*, Academic Press, London, 2016.
20. M.K. Miller, R.G. Forbes, *Atom-Probe Tomography. Local Electrode Atom Probe*, Springer, New York, 2014, pp. 1–423. https://doi.org/10.1007/978-1-4899-7430-3/COVER.
21. H. Zhao, B. Gault, D. Ponge, D. Raabe, and F. De Geuser: *Scr. Mater.*, 2018, vol. 154, pp. 106–10. https://doi.org/10.1016/j.scriptamat.2018.05.024.
22. F. Vurpillot, A. Bostel, and D. Blavette: *Appl. Phys. Lett.*, 2000, vol. 76, pp. 3127–29. https://doi.org/10.1063/1.126545.
23. D.J. Larson, B. Gault, B.P. Geiser, F. De Geuser, and F. Vurpillot: *Curr. Opin. Solid State Mater. Sci.*, 2013, vol. 17, pp. 236–47. https://doi.org/10.1016/j.cossms.2013.09.002.
24. G. Ashiotis, A. Deschildre, Z. Nawaz, J.P. Wright, D. Karkoulis, F.E. Picca, and J. Me Kieffer: *J. Appl. Crystallogr.*, 2015, vol. 48, pp. 510–19. https://doi.org/10.1107/S1600576715004306.
25. J. Kieffer, V. Valls, N. Blanc, and C. Hennig: *J. Synchrotron. Rad.*, 2020, vol. 27, pp. 558–66. https://doi.org/10.1107/S1600577520000776.
26. M. Thuvander, J. Weidow, J. Angseryd, L.K.L. Falk, F. Liu, M. Sonestedt, K. Stiller, and H.O. Andrén: *Ultramicroscopy*, 2011, vol. 111, pp. 604–08. https://doi.org/10.1016/J.ULTRAMIC.2010.12.024.
27. D. Shinde, M. Thuvander, A. Rehan, S. Ejnermark, and K. Stiller: *Microsc. Microanal.*, 2019, vol. 25, pp. 454–61. https://doi.org/10.1017/S1431927619000424.
28. L.M. Pike, I.M. Anderson, C.T. Liu, and Y.A. Chang: *Acta Mater.*, 2002, vol. 50, pp. 3859–79. https://doi.org/10.1016/S1359-6454(02)00192-1.

29. H. Kim, J.Y. Kang, D. Son, T.H. Lee, and K.M. Cho: *Mater. Charact.*, 2015, vol. 107, pp. 376–85. https://doi.org/10.1016/J.MATCHAR.2015.08.001.
30. D. Delagnes, F. Pettinari-Sturmel, M.H. Mathon, R. Danoix, F. Danoix, C. Bellot, P. Lamesle, and A. Grellier: *Acta Mater.*, 2012, vol. 60, pp. 5877–88. https://doi.org/10.1016/J.ACTAMAT.2012.07.030.
31. M.D. Mulholland and D.N. Seidman: *Acta Mater.*, 2011, vol. 59, pp. 1881–97. https://doi.org/10.1016/J.ACTAMAT.2010.11.054.
32. J. Bratberg and K. Frisk: *Metall. Mater. Trans. A Phys. Metall. Mater. Sci.*, 2004, vol. 35A, pp. 3649–63. https://doi.org/10.1007/s11661-004-0271-9.
33. V. Raghavan: *J. Phase Equilib. Diffus.*, 2007, vol. 28, pp. 274–76. https://doi.org/10.1007/S11669-007-9069-Y.
34. M. Filipovic, E. Romhanji, and Z. Kamberovic: *ISIJ Int.*, 2012, vol. 52, pp. 2200–204. https://doi.org/10.2355/isijinternational.52.2200.
35. W.S. Williams: *Mater. Sci. Eng.*, 1988, vol. 105–106, p. 1. https://doi.org/10.1016/0025-5416(88)90474-0.
36. Y. Oba, S. Koppoju, M. Ohnuma, T. Murakami, H. Hatano, K. Sasakawa, A. Kitahara, and J.I. Suzuki: *ISIJ Int.*, 2011, vol. 51, pp. 1852–58. https://doi.org/10.2355/isijinternational.51.1852.
37. V. Gerold and H. Haberkorn: *Phys. Status Solidi*, 1966, vol. 16, pp. 675–84. https://doi.org/10.1002/pssb.19660160234.
38. J. Friedel: *Dislocations*, Pergamon Press, Oxford, 1964.
39. R. Schnitzer, G.A. Zickler, E. Lach, H. Clemens, S. Zinner, T. Lippmann, and H. Leitner: *Mater. Sci. Eng. A*, 2010, vol. 527, pp. 2065–70. https://doi.org/10.1016/J.MSEA.2009.11.046.
40. S.D. Erlach, H. Leitner, M. Bischof, H. Clemens, F. Danoix, D. Lemarchand, and I. Siller: *Mater. Sci. Eng. A*, 2006, vol. 429, pp. 96–106. https://doi.org/10.1016/J.MSEA.2006.05.071.
41. J.P. Adamson and J.W. Martin: *Acta Metall.*, 1971, vol. 19, pp. 1015–18. https://doi.org/10.1016/0001-6160(71)90033-2.
42. Q. Liu and S. Zhao: *MRS Commun.*, 2012, vol. 2, pp. 127–32. https://doi.org/10.1557/mrc.2012.21.
43. Z.B. Jiao, J.H. Luan, M.K. Miller, C.Y. Yu, and C.T. Liu: *Sci. Rep.*, 2016, vol. 61(6), pp. 1–3. https://doi.org/10.1038/srep21364.
44. Z.B. Jiao, J.H. Luan, M.K. Miller, C.Y. Yu, and C.T. Liu: *Acta Mater.*, 2015, vol. 84, pp. 283–91. https://doi.org/10.1016/J.ACTAMAT.2014.10.065.